



Inverted Hartmann mask made by deep X-ray lithography for single-shot multi-contrast X-ray imaging with laboratory setup

ANDREY MIKHAYLOV,^{1,6}  MARGARITA ZAKHAROVA,^{1,6}  VITOR VLNIESKA,² ANKITA KHANDA,¹ SABINE BREMER,^{3,4} MARCUS ZUBER,^{3,4}  SERGIO HENRIQUE PEZZIN,⁵ AND DANAYS KUNKA^{1,*}

¹Institute of Microstructure Technology (IMT), Karlsruhe Institute of Technology (KIT), 76344 Eggenstein-Leopoldshafen, Germany

²Currently at Swiss Federal Laboratories for Materials Science and Technology (EMPA), Überlandstrasse 129, 8600 Dübendorf, Switzerland

³Institute for Photon Science and Synchrotron Radiation Karlsruhe Institute of Technology, Eggenstein-Leopoldshafen D-76344, Germany

⁴Laboratory for Applications of Synchrotron Radiation (LAS), Karlsruhe Institute of Technology, Kaiserstr. 12, Karlsruhe D- 76131, Germany

⁵Center of Technological Sciences, State University of Santa Catarina, R. Paulo Malschitzki, 200 - Zona Industrial Norte, Joinville, SC 89219-710, Brazil

⁶First co-authors with equal contribution

*danays.kunka@kit.edu

Abstract: This paper reports on the fabrication and characterization of an inverted Hartmann mask and its application for multi-contrast X-ray imaging of polymer composite material in a laboratory setup. Hartmann masks open new possibilities for high-speed X-ray imaging, obtaining orientation-independent information on internal structures without rotating the object. The mask was manufactured with deep X-ray lithography and gold electroplating on a low-absorbing polyimide substrate. Such an approach allows us to produce gratings with a small period and high aspect ratio, leading to a higher spatial resolution and extension towards higher X-ray energies. Tuning the manufacturing process, we achieved a homogeneous patterned area without supporting structures, thus avoiding losses on visibility. We tested mask performance in a laboratory setup with a conventional flat panel detector and assessed mask imaging capabilities using a tailored phantom sample of various sizes. We performed multi-modal X-ray imaging of epoxy matrix polymer composites reinforced with glass fibers and containing microcapsules filled with a healing agent. Hartmann masks made by X-ray lithography enabled fast-tracking of structural changes in low absorbing composite materials and of a self-healing mechanism triggered by mechanical stress.

© 2022 Optica Publishing Group under the terms of the [Optica Open Access Publishing Agreement](#)

1. Introduction

Phase-sensitive X-ray imaging techniques serve as a versatile and robust tool for multi-contrast imaging of low absorbing materials. Along with conventional absorption contrast, it allows retrieving phase-contrast and scattering contrast (so-called dark-field or ultra-small angle X-ray scattering) [1–5]. Similar values of the absorption coefficient result in low contrast in the case of absorption-only imaging. Registering phase shifts and scattering signals allows one to extract additional information regarding the inner structure of the specimen.

The most widely used approaches for multi-contrast imaging are based on X-ray interferometry. Since grating-based interferometric X-ray imaging was introduced in 2002 [6], it was used as a highly sensitive tool to study composite materials [7–10], biological samples [3,11–15], optics metrology [5,16,17], etc. Despite the wide use of this method and its high accuracy,

interferometers remain challenging in design and construction. The inability to directly resolve interference patterns and the need for a partially coherent source leads to the use of multiple gratings and a complex positioning system. The production of high-aspect-ratio gratings for grating-based interferometric applications is of separate scientific and engineering interest. Several strategies have been developed to stabilize the grating lamellas, including sunray and bridge designs [18].

The extension of such techniques towards robust and simple setup led to non-interferometric solutions by introducing a single optical element in the beam path. In particular, edge illumination, and later speckle-based X-ray imaging, relaxed spatial coherence requirements for low-brilliance source configurations and faced significant drawbacks in the alignment of absorption masks and mask flux reduction. The restraints of this technique were improved by utilizing single-mask methods, which require the use of specific detectors, thus limiting the detector choice and field of view [19,20]. High-resolution detectors were able to increase the spatial resolution of the system such that the limit becomes the fabrication of small period masks [21]. Speckle methods have also been used to improve flux efficiency with scanning [22] and single-shot [23] implementations. However, spatial resolution once again becomes a limitation in detector pixel size, avoided with scanning instead of phase-stepping [24,25]. Scattering signal can also be difficult to extract in speckle-based imaging [20].

Single-shot phase-contrast and scattering imaging are advantageous in low dose or low flux applications. Consequently, several single-shot imaging approaches emerged: edge-illumination imaging [26], imaging with coded-aperture [27], speckle-based imaging [23], Shack-Hartmann-based imaging [28,29], imaging with Hartmann mask [30–32], and imaging with inverted Hartmann mask [32–34]. However, single-shot grating-based X-ray imaging methods also suffer from interferometric constraints [35]. In simpler implementations, such as edge illumination imaging with an alternating aperture position mask, there is a trade-off between time and noise amplification [36]. The contrast in these systems can also be improved with an alternative setup of vertical mask alignment but at the cost of source utilization efficiency [37].

In the case of single-shot speckle-based X-ray imaging, alignment calibration can be complicated for reference-free measurements. Sensitivity and resolution can be improved with scanning, but it requires extensive data acquisition [22]. Resolution in single-shot speckle-based imaging is also limited by the data subset size choice. While adaptive subsets in Fourier speckle analysis can improve resolution and reduce background noise fluctuations and computation time, small subsets do not see significant improvement [38]. More recently, coded binary phase masks have shown better resolution and performance than speckle-based and grating-based methods as a combination of both techniques and have the potential to be scaled to laboratory sources. Still, they have yet to be implemented [39].

In the last method, the inverted Hartmann Mask is a periodic two-dimensional pattern of gold pillars without supporting structures on a low-absorbing substrate. It has a lower attenuation, which improves the flux efficiency and provides a higher signal-to-noise ratio for measurements, crucial for low-brilliance sources like X-ray tubes [32,33,40,41]. The method showed higher measurement visibility than multi-grating imaging schemes due to lower average absorption [15,42–45].

Inverted Hartmann Mask being introduced in the beam path modulates the wavefront of the incoming wave. Wavefront modulation strongly depends on the percentage of the X-rays absorbed by periodic gold patterns. In the previous paper, we demonstrated the capabilities of phase-contrast imaging with UV lithography-made inverted Hartmann Mask in laboratory setup with the X-ray tube operated at 40 kVp with peak energy of 24 keV [32]. To extend the imaging capabilities of the method towards higher spatial resolution and higher energy applications, we used Deep X-ray lithography as a tool to produce the aforementioned masks with higher pillars and smaller periodicity. Deep X-ray lithography is a well-known technique that allows high

aspect ratio structures patterning over a wide area [46–48]. Recent advances in deep X-ray lithography enable pattern structures down to sub-micrometer sizes [49,50].

As a benchmark, we have performed X-ray multi-contrast imaging of an in-house phantom consisting of polymer pillars and fragments of meshes made by UV lithography (Sections 3.1 and 6.1). In addition, we present results on X-ray imaging of microcapsule-based self-healing polymer composites comparing the behavior before and after dynamic mechanical tests to find evidence of self-healing processes.

2. Inverted Hartmann mask fabrication by deep X-ray lithography

The inverted Hartmann masks (iHM) were produced by adapting the LIGA X-ray process developed at the Institute for Microstructure Technology [51]. The German acronym LIGA stands for lithography, electroplating, and molding (*Lithographie, Galvanik, und Abformung*). LIGA is used to produce and replicate microstructured polymer and metal components with a high aspect ratio. In this work, the process was adapted and finalized with the polymer photoresist stripping after the electroplating stage. The starting template for the lithography mask was a set of arrays of rectangular pillars with different periodicity and areas: 10 μm period over a 2.5 x 2.5 cm area, 8 and 5 μm periods over a 2 x 2 cm areas. Periodic pillar arrays were produced with electron beam lithography (EBPG5200Z, Raith GmbH, Germany) on a 2.7 μm -thick Ti membrane. Feature resolution was inspected using scanning electron microscopy (SEM - Supra VP 60, Carl Zeiss AG, Germany).

As shown in Fig. 1, the starting lithography mask shows no presence of patterning defects. The arrays of gold pillars are consistent in shape and height over the completely patterned area. The measured periods were 5.01, 7.98, and 9.97 μm (measurement error 0.02 μm) with an average pillar height of $4.10 \pm 0.06 \mu\text{m}$ across all periods compared to the designed 4 μm . The inverted Hartmann masks were patterned on low-absorption substrates to ensure a higher signal-to-noise ratio (SNR) without increasing the exposure time during X-ray imaging with low-intensity sources in a laboratory configuration.

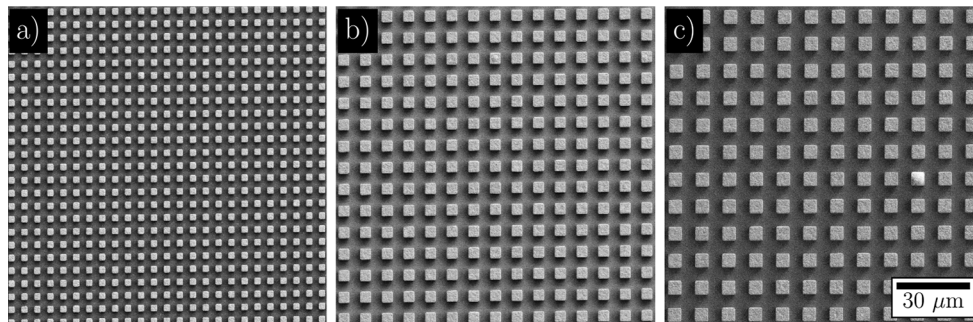


Fig. 1. Scanning electron microscopy images of the lithography mask produced with electron beam lithography: 5 μm period (a), 8 μm period (b), and 10 μm period (c). The scale bar is the same for (a), (b), (c).

A 70 μm -thick layer of the light-sensitive SU8-based negative photoresist formulation mr-X50 (micro resist technology GmbH, Berlin, Germany) was spin-coated onto a 200 μm -thick polyimide substrate (DuPont VespelTM), coated with a CrAu (10/70 nm) conductive layer base for electrodeposition (Fig. 2, steps 1, 2). Soft bake was performed as follows. First, the wafer was slowly heated up to 75 $^{\circ}\text{C}$ and held at this temperature for 1 hour. Second, the wafer was slowly heated up to 95 $^{\circ}\text{C}$ and held at this temperature for 2 hours. Finally, it was cooled down to room temperature for 1 hour (Fig. 2, step 3). The shadow of the pillar array pattern structured the photoresist using deep X-ray radiation (Fig. 2, step 5). Then, the wafer was subjected to

post-exposure bake at 75 °C for 2 hours and afterward cooled overnight. The non-exposed parts were dissolved using the propylenglycolmonomethyl etheracetat organic developer (PGMEA) and rinsed with isopropanol, then dried in a conventional oven for 4 hours (Fig. 2, step 7). In the next

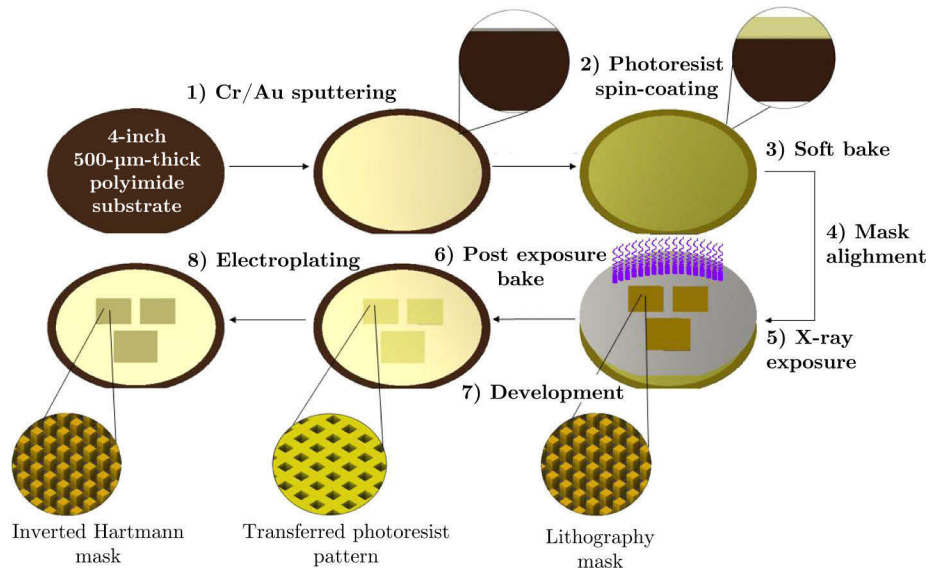


Fig. 2. Deep X-ray lithography schematic sequence for the inverted Hartmann mask manufacturing. X-ray lithography process was carried out at LIGA1 beamline (KARA synchrotron facility, Karlsruhe, Germany).

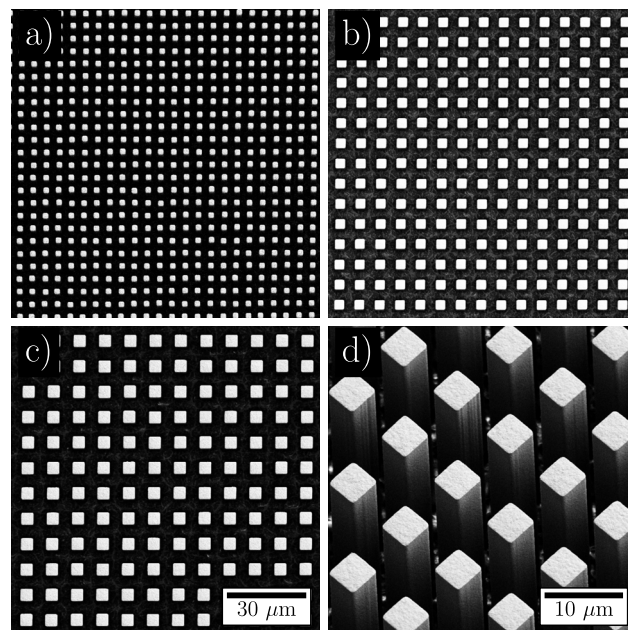


Fig. 3. Scanning electron microscopy images of the inverted Hartmann masks produced with Deep X-ray lithography: 5 μm period (a), 8 μm period (b), 10 μm period (c), isometric view of 10 μm period mask (d). Scale bar for images (a) and (b) shown in the image (c).

step, the cavities of the inverted Hartmann mask pattern structures were filled with gold through an electroplating process (Fig. 2, step 8). Finally, the residual polymer was stripped using oxygen plasma at the temperature of 22°C and power of 1200 W for 30 minutes.

The scanning electron microscopy inspection reveals a homogeneous set of rectangular pillars of 5.11, 7.97, and 9.96 μm (measurement error 0.03 μm) periodicity with a duty cycle of 0.5. The average gold height of the 10 μm period Hartmann mask is $45.92 \pm 0.07 \mu\text{m}$ (Fig. 3).

3. Sample preparation

3.1. Phantom

In order to evaluate the performance of the imaging setup, we have performed the measurements with a phantom sample. The phantom was tailored to simulate a woven polymer composite comprised of glass fibers and microcapsules of various sizes. To mimic the structure of interest with precise control over the structure size, we employed UV lithography to create polymer meshes and pillars of sizes varying from 5 to 100 μm .

Figure 4 shows the outline of the phantom manufacturing process and the images of the microstructures which compose the phantom. The phantom was a tube containing low-absorbing structures (meshes and pillars) of various sizes made by UV lithography. The microstructures were manufactured with negative photoresist (mrX-10, micro resist technology GmbH, Berlin, Germany). The photosensitive polymer layers were spin-coated on three silicon wafers with smooth surface and further exposed with UV light. The cross-linked photoresist patterns were subjected to PGMEA to dissolve the liquid photoresist. The manufactured structures (solid meshes and pillars) of different sizes (5-100 μm) were lifted off the wafers and collected in a small vial. The photoresist pillars were put in first, and most of them were at the bottom of the vial. Some pillars of smaller sizes adhered to the sidewalls of the tube due to electrostatic forces. After the pillars, the micromeshes were folded and placed in the vial.

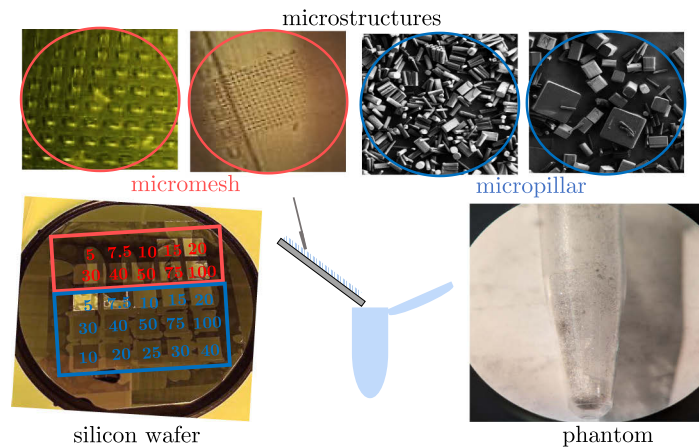


Fig. 4. Phantom manufacturing process. The structures (photoresist meshes and pillars) of different sizes (5-100 μm) were made by UV lithography on a smooth silicon wafer as shown in the lower left corner. Meshes and pillars are outlined in red and blue, respectively. The microstructures were lifted off the wafers and collected in a small vial (Eppendorf tube shown in the lower right corner). On top, the optical microscopy and SEM images of the structures are shown indicating the variability of structure sizes.

3.2. Polymer composite samples

Epoxy resin RenLamM, based on diglycidyl ether of bisphenol A (DGEBA), as well as its hardener (Aradur HY956-2), based on triethyltetramine (TETA), were purchased from Huntsman (Sao Paulo, SP, Brazil). Aminated polydimethylsiloxane (PDMSa), BELSILADM 1650, with viscosity of ca. 1000 mPa·s and amine number of 0.6 mmol·g⁻¹, was kindly provided by Wacker Chemie AG (Burghausen, Bavaria, Germany). Poly(urea-formaldehyde) (PUF) microcapsules filled with the self-healing agent (PDMSa) were produced as described in [52,53]. Plain weave-type E-glass fiber fabric (ABCOL Brasil Compósitos Ltda) with 300 g/m² and density of 2.5 g/cm³ was used as reinforcement.

Epoxy matrix composite specimens were prepared at GRUPOL (UDESC, Brazil) by lamination, using a vacuum bag to create mechanical pressure on the laminate during its cure cycle. Two sample types were produced: 'Reference Composite' (RC), composed of 'plain weave' glass fiber (GF) and epoxy resin (45/55 m/m, with fiber volume fraction of 26 %), and 'Self-healing Composite' (SHC), also composed of GF and DGEBA but with 2.0 wt% of embedded PDMSa-filled PUF microcapsules (fiber volume fraction = 23 %). The samples were produced with dimensions of 15 cm x 15 cm x 1.5 mm and afterwards cut to 35 x 9.5 x 1.5 mm for dynamic mechanical tests and X-ray lithography. RC samples were produced by mixing DGEBA epoxy resin (RenLamM) with the curing agent (Aradur HY956-2) in a 5:1 (m/m) ratio, as recommended by the manufacturer. The reinforcement, four layers of GF fabric, was cut and placed between two layers of Peel Ply and infusion mesh to ensure even distribution of the resin. A vacuum bag fixed with tacky tape was used to cover the mold for the vacuum lamination procedure, as presented in Fig. 5.

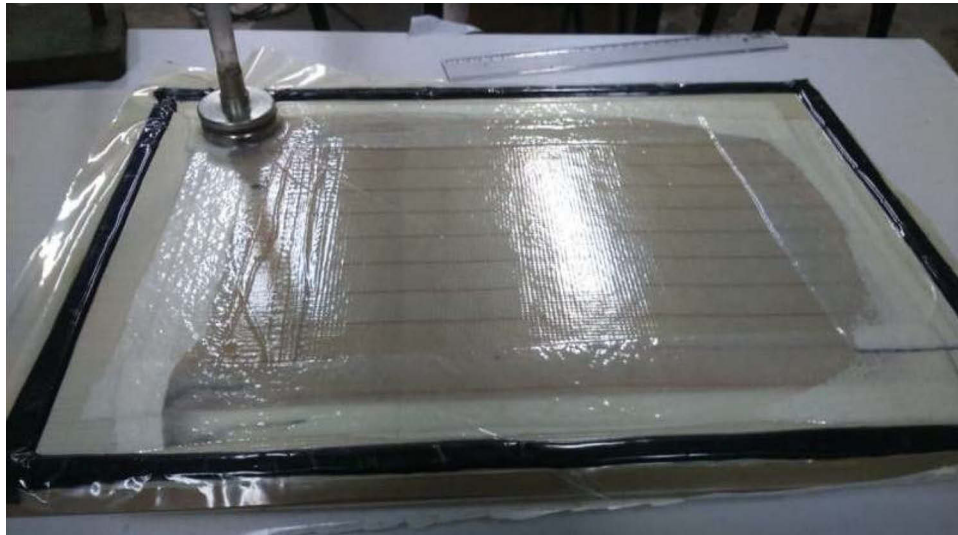


Fig. 5. Preparation of the composite specimens through lamination technique in a vacuum bag.

SHC samples were prepared as follows: filled microcapsules were firstly dispersed in the DGEBA epoxy resin under magnetic stirring for 10 minutes. Afterward, the samples were under negative pressure for 1 hour to remove excess air within the mixture. Then, the hardener was added in a 5:1 (m/m) ratio. The lamination and the vacuum infusion procedures were the same as for RC samples. All samples were cured at room temperature under vacuum for 2 hours, followed by a 24-hour curing period inside the vacuum bag. The laminate was then removed, and

a post-cure step was carried out at 100 °C for 2 hours. In our previous paper we show that only microcapsules with diameter less than 60 μm remain intact after curing [53].

After the post-cure step, dynamic mechanical analyses (DMA) were performed using a Netzsch model DMA 242 equipment (NETZSCH-Gerätebau GmbH, Selb, Germany). The measurements were recorded in the flexural (single cantilever) mode at a frequency of 2 Hz, 10 N force, and an amplitude of 8 μm, in the temperature range from -90°C to 250 °C with a heating rate of 2K·min⁻¹.

4. Experimental setup

X-ray imaging with the inverted Hartmann masks made by DXL was carried out using the X-ray setup at the Computed Lamiography/Computed Tomography Lab of the Institute for Photon Science and Synchrotron Radiation (IPS) at the Karlsruhe Institute of Technology (KIT). The laboratory source was a microfocus X-ray tube (X-RAYWorX) with a tungsten target operated at 60 kV with a target power of 3 W to achieve a focal spot size of approx. 1 μm. Detector unit was a Perkin Elmer XRD 1621 flat panel coupled to a Gadox scintillator, with a 200 μm physical pixel size and a 40 x 40 cm area.

Multi-contrast X-ray imaging with Hartmann masks has already been performed with synchrotron radiation [33,34] and in a laboratory setup [32] with a Medipix detector with 55 μm pixel size. We used a large-area flat panel detector to test whether the method is compatible with accessible imaging detectors used for medical imaging and industrial applications. To achieve the highest spatial resolution with the laboratory setup, we utilized the mask with the 10 μm period, which was placed about 11 mm away from the sources such that the mask period was resolved. The source-detector distance was 150 cm, and the source-object distance for the imaging of the phantom was set to 35 mm and for the imaging of polymer composite to 26 mm. By benefiting from the magnification offered by the X-ray tube, the mask magnification of 140X and the projected period of 1400 μm were achieved. This resulted in the sampling of 7 pixels per mask period.

The setup parameters were optimized as proposed in [13] in order to minimize the penumbral blur:

$$\frac{s}{P} \cdot \frac{D_2 + D_3}{D_1 + D_2 + D_3} \ll 1, \quad (1)$$

and avoid phase wraparound artefacts:

$$\frac{s}{P} \cdot \frac{D_1 D_3}{(D_1 + D_2)(D_1 + D_2 + D_3)} > 1, \quad (2)$$

where s is the focal spot size of the X-ray tube, P is the period of the iHM, D_1 , D_2 , and D_3 are the distances from the source to iHM, from iHM to the object, and from the object to the detector, respectively (Fig. 6). The optimization criteria were bounded by the condition that the projected mask period has to be resolved:

$$D_1 < \frac{(D_1 + D_2 + D_3) \cdot P}{3 \cdot s}. \quad (3)$$

The optimization of the setup was formulated as a minimization of the difference of Eq. (1) and Eq. (2) criteria with the bounding conditions according to Eq. (3). The penumbral blur at the detector plane for the mask was approx. 150 μm. For the imaging with the object, the penumbral blur for the phantom and the polymer composite was 32 and 75 μm, respectively. Considering the physical pixel size of 200 μm, the effect of blurring on the spatial resolution for the mask and the object in the setup can be neglected.

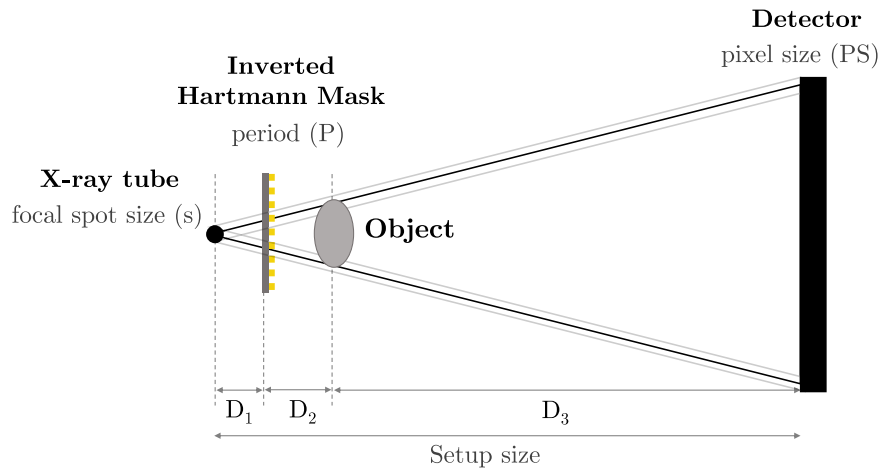


Fig. 6. Experimental laboratory setup with mask-before-sample geometry. X-rays are emitted from the X-ray tube with focal spot size s . The inverted Hartmann mask with period P is located at the distance D_1 from the source. The detector with physical pixel size PS records the overlapped iHM-object image. Gray divergent lines highlight the penumbral blur introduced by the extended source.

The spatial resolution of the setup is defined as the period of the mask projected onto the object under investigation. The phase detection limit in such a setup can be estimated from the setup parameters and noise level in differential phase-contrast images as follows:

$$\alpha_{min} = \frac{PS(D_1 + D_2)}{D_3(D_1 + D_2 + D_3)} \cdot I_{noise}, \quad (4)$$

where α_{min} is the minimum detectable refraction angle, PS is the pixel size, D_1 , D_2 and D_3 are the distances in the setup (see Fig. 6), and I_{noise} is defined as the standard deviation of the signal in the background (area outside the sample) for differential phase-contrast images.

5. X-ray imaging with the inverted Hartmann mask

Visibility measurements, imaging of the phantom (vial with microstructures) and polymer composite samples were performed using the setup described in Section 4. We used the Fourier analysis approach [30] to obtain three contrast modalities: absorption, differential phase, and scattering in two orthogonal directions. From the two differential phase images in orthogonal directions, the phase map was reconstructed using the Frankot-Chellappa approach [54,55]. Background subtraction compensated for the distortion introduced by the cone-beam artifacts. For highly absorbing samples imaged with polychromatic radiation, cross-talk between absorption and scattering signals due to beam hardening [56] has been reported [57]. To suppress this effect for the phantom sample, linear decorrelation of the absorption and the scattering images was performed [58,59].

5.1. Visibility measurements

To assess wavefront modulation performance of the produced inverted Hartmann masks, visibility measurements were carried out. Visibility was defined as follows:

$$V = \frac{I_{max} - I_{min}}{I_{max} + I_{min}}, \quad (5)$$

where I_{\max} and I_{\min} are the local maximum and minimum intensities. Figure 7(a) shows a projection of the full region-of-interest and close-up of the iHM pattern. Projected spots are well resolved and show sufficient wavefront modulation. Figure 7(b) presents the visibility map with the average visibility value of 0.46, which is higher than the average visibility range in case of grating-based interferometry (0.1-0.3) [43–45]. However, the visibility is not uniform over the field of view: lower visibility areas are caused by the cone-beam effect due to the short range proximity between iHM and source.

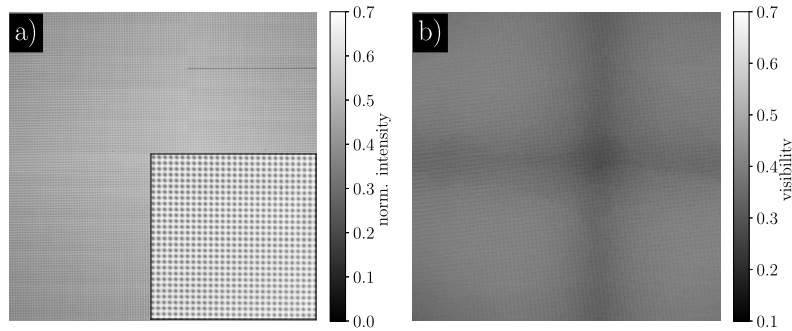


Fig. 7. Inverted Hartmann mask raw projection with close-up (a) and visibility map (b).

5.2. Phase-contrast imaging of the phantom

In the imaging setup described in Section 4, the X-ray imaging of the phantom specimen was performed. The distance between the source and the phantom was 35 mm; both the micromeshes and the micropillars were in the field of view. The spatial resolution of the setup was $30 \mu\text{m}$ and the phase detection limit $0.16 \mu\text{rad}$ (Eq. (4)).

Figure 8(a) is the overlapped projections of the phantom and the periodic mask normalized by the background. The darker area in the lower part of the vial is the hot glue that fixed the phantom on the holder. Figure 8(b) represents the absorption image. The phase map shown in Figure 8(c) was reconstructed using the differential phase-contrast images in horizontal and vertical directions. Figures 8(e) and (f) display the scattering contrasts in two directions. The scattering information was also averaged over two directions to illustrate the location of the structures with sizes below the resolution of the imaging setup (Fig. 8(d)).

In Fig. 8, one can see how different contrast modalities provide information on various sample features. The absorption image has a low signal from the microstructures: the mesh inside and the micropillars are barely distinguishable from the hot glue. In the phase map (Fig. 8(c)), one can observe the vertical lines of the mesh while the horizontal lines are not visible. As the mesh period is at the limit of the achieved resolution, it also appears in the scattering images. In both phase and scattering images, there is a change in the signal where the micropillars are concentrated (indicated by the black arrow in Fig. 8(e)). There is a strong scattering signal from the hot glue. Microbubbles in the glue or an unsuppressed cross-talk between the absorption and the scattering signal can explain such an increase.

Figure 9 shows the absorption (a) and the differential phase-contrast images in the horizontal (d) and the vertical (g) directions. Along the blue and red lines indicated in the images, the profiles are plotted for the micromesh (red) and the micropillar (blue) locations. The profile for the horizontal differential phase contrast (Fig. 9(e)) reveals the periodic nature of the signal obtained from the micromesh with a periodicity of $60 \mu\text{m}$. The profile in the area where the micropillars were concentrated (blue line) also shows the change in the signal, indicating the presence of a refractive object. For all profiles in Fig. 9, the SNR values were defined for the

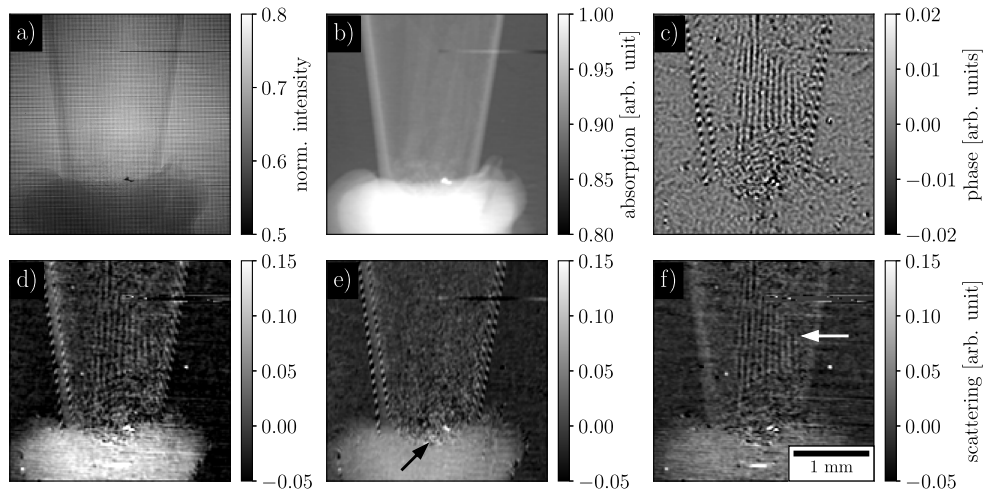


Fig. 8. Imaging of the phantom sample: (a) - raw projection, (b) - absorption, (c) - phase map, (d) - sum of scattering signal, (e,f) - scattering in vertical and horizontal directions. The black arrow indicates the location of the micropillars and the white arrow the location of the micromeshes.

phase shift introduced by the micromeshes or the micropillars compared to the background signal outside of the vial:

$$SNR = 10 \log_{10} \left(\frac{\max(|S|)}{\text{mean}(|S|)} \right), \quad (6)$$

where $\max(S)$ and $\text{mean}(S)$ indicate the maximum and mean intensity of signal S (gray value) in the profile.

A similar increase in the signal is observed for the micropillars and the micromeshes (SNR between 6.8 and 8.2) since they are composed of the same epoxy-based photosensitive polymer treated in the same conditions (same refractive index). The vial walls introduced the highest phase shift (SNR = 9.2). There is a signal increase for the differential images in both directions due to the random orientations of the micropillars, but with higher background signal (Fig. 9(f)) due to the refraction from the hot glue border. One can see that there is no strong alternation of the vertical differential phase-contrast image for the area where the mesh is located. The reason could be the misalignment between the horizontal mesh lines as the mesh was folded horizontally and placed inside the vial.

5.3. Phase-contrast imaging of the polymer composite materials

For the X-ray imaging of the polymer composite materials, distance of 26 mm between the source and the object was chosen. Spatial resolution, defined by projected period of the inverted Hartmann mask, was $24 \mu\text{m}$ and the phase detection limit $0.06 \mu\text{rad}$ (Eq. (4)).

Figure 10 shows multi-contrast X-ray imaging with the inverted Hartman mask of the RC sample (Figs. 10(a),(b),(e),(f)) and the RC sample after DMA (Figs. 10(c),(d),(g),(h)). Images in the absorption contrast reveal the tailored structure of the RC sample, evidencing the glass fiber fabric used as reinforcement (Figs. 10(a),(c)). Bright areas on the absorption images correspond to the overlaid bundles. Due to the routine of the FFT analysis in multi-contrast X-ray imaging, absorption and scattering signals of the highly absorbing specimens could be correlated [58,60]. In the presented measurements, maximum absorption is 30 % with mean value of 22 ± 4 % and the thickness of polymer composite samples were ca. 3 mm. Decorrelation procedure was performed according to [58] resulting in negligible changes.

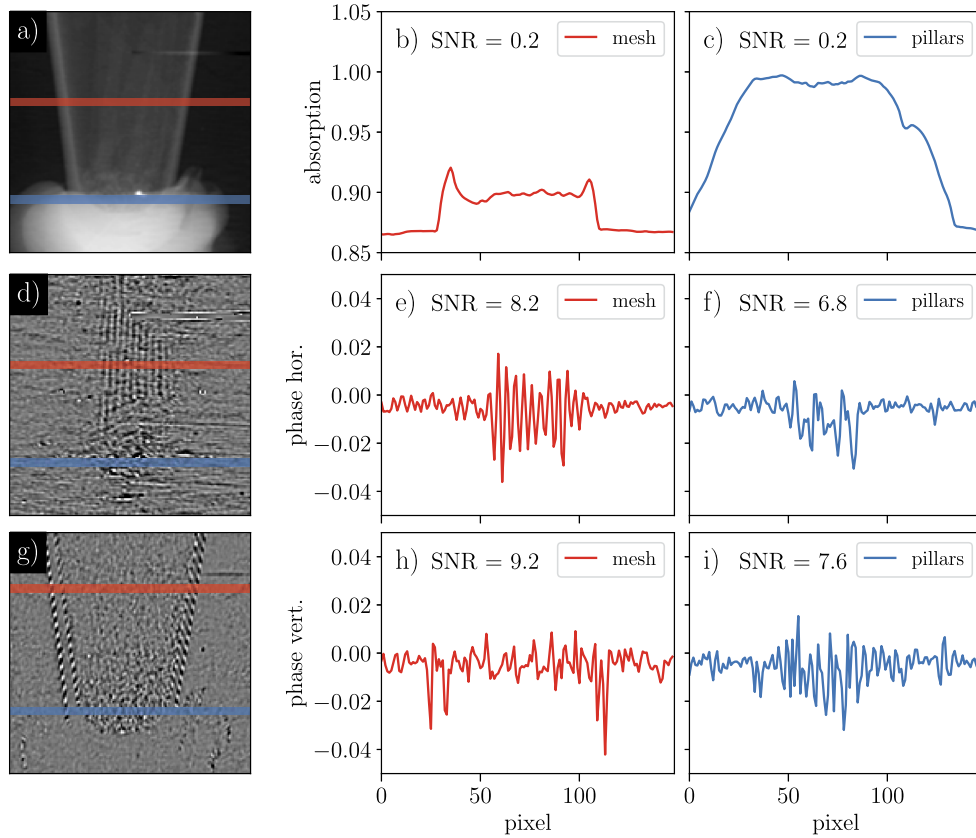


Fig. 9. (a) - absorption contrast; (d,g) - differential phase contrast in horizontal and vertical directions; (b,e,h) - profiles for the mesh locations outlined with red lines; (c,f,i) - profiles for the micropillars locations outlined with blue lines. The SNR value is introduced for comparison of the signals according to Eq. (6).

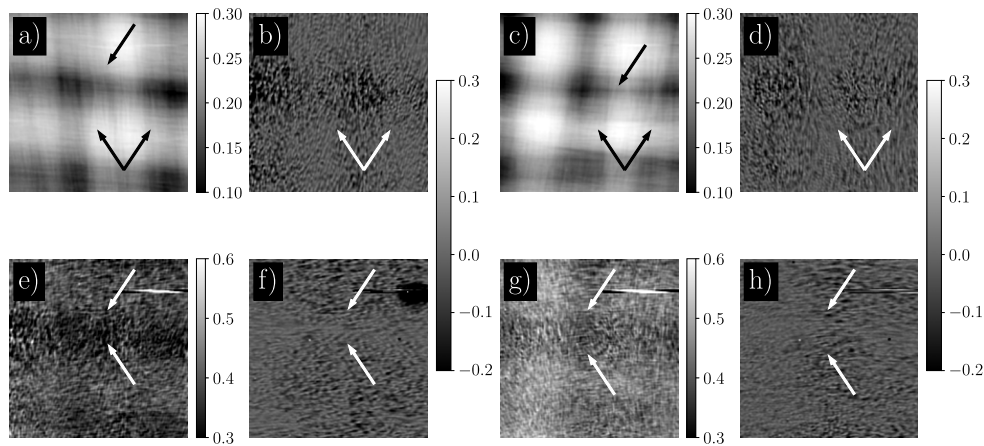


Fig. 10. Multi-contrast X-ray imaging of the reference samples (a,b,e,f) and reference samples after DMA (c,d,g,h). The figures show absorption contrast (a,c); differential phase in vertical direction (b,d); scattering (e,g); differential phase in horizontal direction (f,h).

RC samples before and after dynamic mechanical analysis do not show a significant difference in the mean absorption signal (Table 1). Dynamic mechanical tests did not induce any changes in the mean absorption of the sample nor a significant impact on the fiber distribution. One can see the distribution of the microfiber bundles oriented orthogonally to each other. However, it is visible that borders of vertical microfiber bundles are less defined (lower arrows in Figs. 10(a),(c)) than horizontal. Diverging microfibers in the vertical gaps between bundles result in smearing of the absorption. On the other side, gaps containing less material would be more prominent on the differential phase and scattering images.

Due to the directional sensitivity of the differential phase measurements with the inverted Hartmann mask, one could notice complementary areas of high intensity in Figs. 10(a),(b),(f)) for the reference sample and Figs. 10(c),(d),(h)) for the RC after dynamic mechanical analysis. Figures 10(b),(d)) reveal vertical refraction patterns corresponding to the vertical gaps of the microfiber bundles (marked with arrows). Similarly, in Figs. 10(f),(h), one could notice horizontal patterns corresponding to the horizontal gaps. In addition, in Figs. 10(e),(g), there are horizontal and vertical patterns of lower average signal and brighter spots complementary to the absorption. This could be explained by the nature of the scattering and the differential phase contrast in multi-contrast X-ray imaging with inverted Hartmann masks. Scattering contrast could be interpreted as a refraction signal below the angular resolution of the setup. High absorption areas, containing microfibers in both directions, could not be well resolved in the differential phase measurements unlike in the scattering. On the other hand, separated diverging microfibers in the vertical and horizontal gaps result in vertical and horizontal patterns in the differential phase.

Table 1. Mean absorption and scattering value in arbitrary unit for the RC and SHC samples, before and after dynamic mechanical analysis (DMA).

Sample	Mean absorption, ± 0.04	Mean scattering, ± 0.03
RC	0.22	0.38
RC after DMA	0.22	0.44
SHC	0.22	0.43
SHC after DMA	0.22	0.40

Mean scattering signal in case of the reference sample (Fig. 10(e)) is slightly lower than mean scattering signal in the RC after mechanical testing (Fig. 10(g)) with values of 0.38 ± 0.03 and 0.44 ± 0.03 , respectively (Table 1). This could be considered a result of X-ray scattering on the microfractures of glass microfibers and polymer matrix formed under mechanical stress.

Figure 11 shows multi-contrast X-ray imaging of SHC samples before (Fig. 11(a),(b),(e),(f)) and after dynamic mechanical analysis (Fig. 11(c),(d),(g),(h)).

Similarly to RC samples, there are no changes in mean absorption values (Table 1). However, one could see that the microfiber bundles are more even and have well-defined borders. It was not possible to resolve microcapsules directly due to their size distribution after curing [53].

Differential phase images of SHC samples before (Figs. 11(b),(f)) and after dynamic mechanical analysis (Fig. 11(d),(h)) are in good accordance with absorption images (Figs. 11(a),(c)); it is possible to notice vertical and horizontal stripes corresponding to the gaps between the bundles (marked with arrows). A similar pattern could be observed in the scattering images (Figs. 11(e),(g)).

Mean scattering signal in the case of the sample with the microcapsules is higher in comparison to the reference with mean values of 0.43 ± 0.03 and 0.38 ± 0.03 , respectively. This can be interpreted as scattering on the microcapsules acting as scattering centers. There is no significant change in the mean scattering signal after the induced stress for the SHC samples (Table 1). However, the RC sample exhibits higher scattering after dynamic mechanical analysis, which

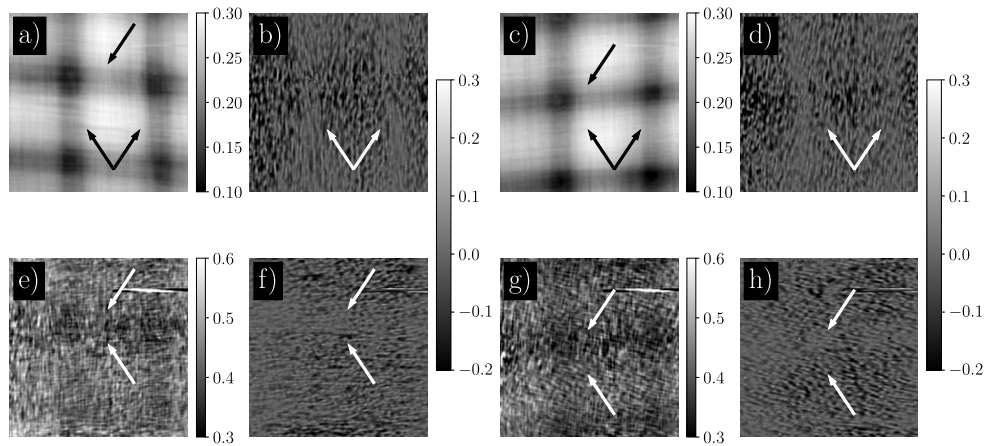


Fig. 11. Multi-contrast X-ray imaging of the samples embedded with microcapsules (a,b,e,f) and sample embedded with microcapsules after DMA (c,d,g,h). The figures show absorption contrast (a,c); differential phase vertical direction (b,d); scattering (e,g); differential phase horizontal direction (f,h).

can be associated with microfiber fracture. This could be explained by the stress-triggered self-healing mechanism [52,53]. Micro-fractions that have appeared during dynamic mechanical tests were filled by the healing agent (PDMSa) released from the broken microcapsules, leading to a decreased amount of scattering centers.

6. Conclusion

In this article, we presented the results of laboratory-based phase-contrast X-ray imaging utilizing the inverted Hartmann mask. Adapting the LIGA technology allowed us to manufacture the iHM on a low-absorbing polyimide substrate, which does not introduce beam hardening. We obtained the homogeneous arrays of gold pillars with periods of 5.11 ± 0.03 , 7.97 ± 0.03 , and $9.96 \pm 0.03 \mu\text{m}$ and height up to $45.92 \pm 0.07 \mu\text{m}$ without supporting structures. The gold pillars of homogeneous height significantly attenuate the polychromatic radiation emitted by the X-ray tube with a broad energy spectrum up to 60 keV. A combination of high gold pillars and low-absorbing substrate ensures sufficient wavefront modulation and high mask visibility (0.46) in a laboratory environment.

A customized phantom sample comprised of micromeshes and micropillars was made by UV lithography to mimic the polymer composite structure. Differential phase-contrast images revealed sensitivity to periodic mesh structures and micropillars. Compared to absorption contrast, differential phase-contrast images provided a significantly higher SNR for the signal coming from polymer microstructures. An increase in the scattering contrast also indicated the areas of microstructure concentration.

Multi-contrast X-ray imaging with the inverted Hartmann mask was used to study glass microfiber reinforced polymer composite samples with self-healing properties under mechanical stress. The absorption and the differential phase-contrast images revealed the tailored structure of the designed polymer composites. It was possible to observe the distribution of glass microfibers. Scattering contrast imaging modality showed the changes in the inner structure of the polymer composites below the spatial and the angular resolution limits. Mechanical stress measurement and the introduction of microcapsules with the healing agent resulted in new scattering centers, which contributed to the mean scattering signal. The uniform signal increase indicated microfracture propagation and microcapsule distribution uniformity over the sample

area. In addition, it was possible to track the self-healing mechanism of the polymer composite material under mechanical stress.

Acknowledgments. This work was carried out with the support of the Karlsruhe Nano Micro Facility (KNMFi). The authors acknowledge the funding of the Karlsruhe School of Optics and Photonics (KSOP), associated institution at KIT, and the Karlsruhe House of Young Scientists (KHYS). We acknowledge support by the KIT-Publication Fund of the Karlsruhe Institute of Technology.

Disclosures. The authors declare no conflicts of interest.

Data availability. Data underlying the results presented in this paper are not publicly available at this time but may be obtained from the authors upon reasonable request.

References

1. T. Davis, D. Gao, T. Gureyev, A. Stevenson, and S. Wilkins, "Phase-contrast imaging of weakly absorbing materials using hard x-rays," *Nature* **373**(6515), 595–598 (1995).
2. A. Momose, S. Kawamoto, I. Koyama, Y. Hamaishi, K. Takai, and Y. Suzuki, "Demonstration of x-ray talbot interferometry," *Jpn. J. Appl. Phys.* **42**(Part 2, No. 7B), L866 (2003).
3. T. Weitkamp, A. Diaz, C. David, F. Pfeiffer, M. Stamparoni, P. Cloetens, and E. Ziegler, "X-ray phase imaging with a grating interferometer," *Opt. Express* **13**(16), 6296–6304 (2005).
4. F. Pfeiffer, M. Bech, O. Bunk, P. Kraft, E. F. Eikenberry, C. Brönnimann, C. Grünzweig, and C. David, "Hard-x-ray dark-field imaging using a grating interferometer," *Nat. Mater.* **7**(2), 134–137 (2008).
5. F. Koch, F. O'Dowd, M. Cardoso, R. Da Silva, M. Cavicchioli, S. Ribeiro, T. Schröter, A. Faisal, P. Meyer, D. Kunka, and J. Mohr, "Low energy x-ray grating interferometry at the brazilian synchrotron," *Opt. Commun.* **393**, 195–198 (2017).
6. C. David, B. Nöhammer, H. Solak, and E. Ziegler, "Differential x-ray phase contrast imaging using a shearing interferometer," *Appl. Phys. Lett.* **81**(17), 3287–3289 (2002).
7. S. Senck, M. Scheerer, V. Revol, K. Dobes, B. Plank, and J. Kastner, "Non-destructive evaluation of defects in polymer matrix composites for aerospace applications using x-ray talbot-lau interferometry and micro ct," in *58th AIAA/ASCE/AHS/ASC Structures, Structural Dynamics, and Materials Conference*, (2017), p. 0355.
8. F. Prade, F. Schaff, S. Senck, P. Meyer, J. Mohr, J. Kastner, and F. Pfeiffer, "Nondestructive characterization of fiber orientation in short fiber reinforced polymer composites with x-ray vector radiography," *NDT&E Int.* **86**, 65–72 (2017).
9. N. Morimoto, K. Kimura, T. Shirai, T. Doki, S. Sano, A. Horiba, and K. Kitamura, "Talbot-lau interferometry-based x-ray imaging system with retractable and rotatable gratings for nondestructive testing," *Rev. Sci. Instrum.* **91**(2), 023706 (2020).
10. J. Glinz, J. Šleichrt, D. Kytýř, S. Ayalur-Karunakaran, S. Zabler, J. Kastner, and S. Senck, "Phase-contrast and dark-field imaging for the inspection of resin-rich areas and fiber orientation in non-crimp vacuum infusion carbon-fiber-reinforced polymers," *J. Mater. Sci.* **56**(16), 9712–9727 (2021).
11. F. Pfeiffer, T. Weitkamp, O. Bunk, and C. David, "Phase retrieval and differential phase-contrast imaging with low-brilliance x-ray sources," *Nat. Phys.* **2**(4), 258–261 (2006).
12. T. Weitkamp, C. David, O. Bunk, J. Bruder, P. Cloetens, and F. Pfeiffer, "X-ray phase radiography and tomography of soft tissue using grating interferometry," *Eur. J. Radiol.* **68**, S13–S17 (2008).
13. E. E. Bennett, R. Kopace, A. F. Stein, and H. Wen, "A grating-based single-shot x-ray phase contrast and diffraction method for in vivo imaging," *Med. Phys.* **37**(11), 6047–6054 (2010).
14. L. B. Gromann, F. De Marco, K. Willer, P. B. Noël, K. Scherer, B. Renger, B. Gleich, K. Achterhold, A. A. Fingerle, D. Muenzel, S. Auweter, K. Hellbach, M. Reiser, A. Baehr, M. Dmochewicz, T. J. Schroeter, F. J. Koch, P. Meyer, D. Kunka, J. Mohr, A. Yaroshenko, H.-I. Maack, T. Pralow, H. van der Heijden, R. Proksa, T. Koehler, N. Wieberneit, K. Rindt, E. J. Rummeny, F. Pfeiffer, and J. Herzen, "In-vivo x-ray dark-field chest radiography of a pig," *Sci. Rep.* **7**(1), 1–7 (2017).
15. M. Seifert, V. Ludwig, M. Gallersdörfer, C. Hauke, K. Hellbach, F. Horn, G. Pelzer, M. Radicke, J. Rieger, S.-M. Sutter, T. Michel, and G. Anton, "Single-shot talbot-lau x-ray dark-field imaging of a porcine lung applying the moiré imaging approach," *Phys. Med. Biol.* **63**(18), 185010 (2018).
16. G. Mana, "Applications of x-ray interferometry in metrology and phase-contrast imaging," in *Seventh International Symposium on Laser Metrology Applied to Science, Industry, and Everyday Life*, vol. 4900 (International Society for Optics and Photonics, 2002), pp. 257–268.
17. T. Weitkamp, B. Nöhammer, A. Diaz, C. David, and E. Ziegler, "X-ray wavefront analysis and optics characterization with a grating interferometer," *Appl. Phys. Lett.* **86**(5), 054101 (2005).
18. J. Mohr, T. Grund, D. Kunka, J. Kenntner, J. Leuthold, J. Meiser, J. Schulz, and M. Walter, "High aspect ratio gratings for x-ray phase contrast imaging," in *AIP Conference proceedings*, vol. 1466 (American Institute of Physics, 2012), pp. 41–50.
19. E. S. Dreier, C. Silvestre, J. Kehres, D. Turecek, M. Khalil, J. Hemmingsen, O. Hansen, J. Jakubek, R. Feidenhans, and U. Olsen, "Virtual subpixel approach for single-mask phase-contrast imaging using timepix3," *J. Instrum.* **14**(1), C01011 (2019).

20. A. Olivo, "Edge-illumination x-ray phase-contrast imaging," *J. Physics: Condens. Matter* **33**, 363002 (2021).
21. A. Pil-Ali, S. Adnani, C. C. Scott, and K. S. Karim, "Evaluation of edge-illumination and propagation-based x-ray phase contrast imaging methods for high resolution imaging application," in *Medical Imaging 2021: Physics of Medical Imaging*, vol. 11595 (International Society for Optics and Photonics, 2021), p. 115951N.
22. S. Berujon, H. Wang, and K. Sawhney, "X-ray multimodal imaging using a random-phase object," *Phys. Rev. A* **86**(6), 063813 (2012).
23. K. S. Morgan, D. M. Paganin, and K. K. Siu, "X-ray phase imaging with a paper analyzer," *Appl. Phys. Lett.* **100**(12), 124102 (2012).
24. A. Astolfo, M. Endrizzi, F. A. Vittoria, P. C. Diemoz, B. Price, I. Haig, and A. Olivo, "Large field of view, fast and low dose multimodal phase-contrast imaging at high x-ray energy," *Sci. Rep.* **7**(1), 1–8 (2017).
25. I. Zanette, T. Zhou, A. Burvall, U. Lundström, D. H. Larsson, M. Zdora, P. Thibault, F. Pfeiffer, and H. M. Hertz, "Speckle-based x-ray phase-contrast and dark-field imaging with a laboratory source," *Phys. Rev. Lett.* **112**(25), 253903 (2014).
26. A. Olivo, F. Arfelli, G. Cantatore, R. Longo, R. H. Menk, S. Pani, M. Prest, P. Poropat, L. Rigon, G. Tromba, E. Vallazza, and E. Castelli, "An innovative digital imaging set-up allowing a low-dose approach to phase contrast applications in the medical field," *Med. Phys.* **28**(8), 1610–1619 (2001).
27. A. Olivo and R. Speller, "A coded-aperture technique allowing x-ray phase contrast imaging with conventional sources," *Appl. Phys. Lett.* **91**(7), 074106 (2007).
28. T. dos Santos Rolo, S. Reich, D. Karpov, S. Gasilov, D. Kunka, E. Fohtung, T. Baumbach, and A. Plech, "A shack-hartmann sensor for single-shot multi-contrast imaging with hard x-rays," *Appl. Sci.* **8**(5), 737 (2018).
29. A. Mikhaylov, S. Reich, M. Zakharova, V. Vlnieska, R. Laptev, A. Plech, and D. Kunka, "Shack-hartmann wavefront sensors based on 2d refractive lens arrays and super-resolution multi-contrast x-ray imaging," *J. Synchrotron Radiat.* **27**(3), 788–795 (2020).
30. H. H. Wen, E. E. Bennett, R. Kopace, A. F. Stein, and V. Pai, "Single-shot x-ray differential phase-contrast and diffraction imaging using two-dimensional transmission gratings," *Opt. Lett.* **35**(12), 1932–1934 (2010).
31. K. S. Morgan, D. M. Paganin, and K. K. Siu, "Quantitative single-exposure x-ray phase contrast imaging using a single attenuation grid," *Opt. Express* **19**(20), 19781–19789 (2011).
32. M. Zakharova, S. Reich, A. Mikhaylov, V. Vlnieska, M. Zuber, S. Engelhardt, T. Baumbach, and D. Kunka, "A comparison of customized hartmann and newly introduced inverted hartmann masks for single-shot phase-contrast x-ray imaging," in *EUV and X-ray Optics: Synergy between Laboratory and Space VI*, vol. 11032 (International Society for Optics and Photonics, 2019), p. 110320U.
33. M. Zakharova, S. Reich, A. Mikhaylov, V. Vlnieska, T. dos Santos Rolo, A. Plech, and D. Kunka, "Inverted hartmann mask for single-shot phase-contrast x-ray imaging of dynamic processes," *Opt. Lett.* **44**(9), 2306–2309 (2019).
34. M. Zakharova, A. Mikhaylov, V. Vlnieska, and D. Kunka, "Single-shot multicontrast x-ray imaging for in situ visualization of chemical reaction products," *J. Imaging* **7**(11), 221 (2021).
35. T. Inoue, S. Matsuyama, S. Kawai, H. Yumoto, Y. Inubushi, T. Osaka, I. Inoue, T. Koyama, K. Tono, H. Ohashi, M. Yabashi, T. Ishikawa, and K. Yamauchi, "Systematic-error-free wavefront measurement using an x-ray single-grating interferometer," *Rev. Sci. Instrum.* **89**(4), 043106 (2018).
36. Y. Chen, W. Zhou, C. K. Hagen, A. Olivo, and M. A. Anastasio, "Comparison of data-acquisition designs for single-shot edge-illumination x-ray phase-contrast tomography," *Opt. Express* **28**(1), 1–19 (2020).
37. C. Zhang, X. Pan, H. Shang, and G. Li, "Alternative edge illumination set-up for single-shot x-ray phase contrast imaging," *J. Appl. Phys.* **124**(16), 164906 (2018).
38. N. Tian, H. Jiang, A. Li, D. Liang, and F. Yu, "High-precision speckle-tracking x-ray imaging with adaptive subset size choices," *Sci. Rep.* **10**(1), 1–12 (2020).
39. Z. Qiao, X. Shi, M. J. Wojcik, L. Rebuffi, and L. Assoufid, "Single-shot x-ray phase-contrast and dark-field imaging based on coded binary phase mask," *Appl. Phys. Lett.* **119**(1), 011105 (2021).
40. M. Zakharova, V. Vlnieska, H. Fornasier, M. Börner, T. d. S. Rolo, J. Mohr, and D. Kunka, "Development and characterization of two-dimensional gratings for single-shot x-ray phase-contrast imaging," *Appl. Sci.* **8**(3), 468 (2018).
41. A. Gustschin, M. Riedel, K. Taphorn, C. Petrich, W. Gottwald, W. Noichl, M. Busse, S. E. Francis, F. Beckmann, J. U. Hammel, J. Moosmann, P. Thibault, and J. Herzen, "High-resolution and sensitivity bi-directional x-ray phase contrast imaging using 2d talbot array illuminators," *Optica* **8**(12), 1588–1595 (2021).
42. I. Zanette, T. Weitkamp, T. Donath, S. Rutishauser, and C. David, "Two-dimensional x-ray grating interferometer," *Phys. Rev. Lett.* **105**(24), 248102 (2010).
43. J. Vila-Comamala, L. Romano, V. Guzenko, M. Kagias, M. Stampanoni, and K. Jefimovs, "Towards sub-micrometer high aspect ratio x-ray gratings by atomic layer deposition of iridium," *Microelectron. Eng.* **192**, 19–24 (2018).
44. L. Romano, J. Vila-Comamala, K. Jefimovs, and M. Stampanoni, "High-aspect-ratio grating microfabrication by platinum-assisted chemical etching and gold electroplating," *Adv. Eng. Mater.* **22**, 2000258 (2020).
45. J. Vila-Comamala, L. Romano, K. Jefimovs, H. Dejea, A. Bonnin, A. C. Cook, I. Planinc, M. Cikes, Z. Wang, and M. Stampanoni, "High sensitivity x-ray phase contrast imaging by laboratory grating-based interferometry at high talbot order geometry," *Opt. Express* **29**(2), 2049–2064 (2021).
46. V. Saile, U. Wallrabe, O. Tabata, and J. G. Korvink, *LIGA and its Applications*, vol. 7 (Wiley Online Library, 2009).
47. H. Guckel, "High-aspect-ratio micromachining via deep x-ray lithography," *Proc. IEEE* **86**(8), 1586–1593 (1998).

48. J. M. Park, J. H. Kim, J. S. Han, D. S. Shin, S. C. Park, S. H. Son, and S. J. Park, "Fabrication of tapered micropillars with high aspect-ratio based on deep x-ray lithography," *Materials* **12**(13), 2056 (2019).
49. T. Mappes, S. Achenbach, and J. Mohr, "Process conditions in x-ray lithography for the fabrication of devices with sub-micron feature sizes," *Microsyst. Technol.* **13**(3-4), 355–360 (2007).
50. A. Faisal, T. Beckenbach, J. Mohr, and P. Meyer, "Influence of secondary effects in the fabrication of submicron resist structures using deep x-ray lithography," *J. Micro/Nanolith. MEMS MOEMS* **18**(2), 023502 (2019).
51. E. Backer, W. Ehrfeld, D. Münchmeyer, H. Betz, A. Heuberger, S. Pongratz, W. Glashauser, H. Michel, and R. v. Siemens, "Production of separation-nozzle systems for uranium enrichment by a combination of x-ray lithography and galvanoplastics," *Naturwissenschaften* **69**(11), 520–523 (1982).
52. W. R. Weiermann, M. M. Meier, and S. H. Pezzin, "Microencapsulated amino-functional polydimethylsiloxane as autonomous external self-healing agent for epoxy systems," *J. Appl. Polym. Sci.* **136**, 47627 (2019).
53. S. F. Da Costa, M. Zuber, M. Zakharova, A. Mikhaylov, T. Baumbach, D. Kunka, and S. H. Pezzin, "Self-healing triggering mechanism in epoxy-based material containing microencapsulated amino-polysiloxane," *Nano Select*, early access (2021).
54. S. Marathe, L. Assoufid, X. Xiao, K. Ham, W. W. Johnson, and L. G. Butler, "Improved algorithm for processing grating-based phase contrast interferometry image sets," *Rev. Sci. Instrum.* **85**(1), 013704 (2014).
55. W. Grizolli, X. Shi, L. Assoufid, and L. G. Butler, "Wavepy-python package for x-ray grating interferometry with applications in imaging and wavefront characterization," in *AIP Conference Proceedings*, vol. 2054 (AIP Publishing LLC, 2019), p. 060017.
56. G. Pelzer, G. Anton, F. Horn, J. Rieger, A. Ritter, J. Wandner, T. Weber, and T. Michel, "A beam hardening and dispersion correction for x-ray dark-field radiography," *Med. Phys.* **43**(6Part1), 2774–2779 (2016).
57. E. A. Miller, T. A. White, B. S. McDonald, and A. Seifert, "Phase contrast x-ray imaging signatures for security applications," *IEEE Trans. Nucl. Sci.* **60**(1), 416–422 (2013).
58. S. Kaeppeler, F. Bayer, T. Weber, A. Maier, G. Anton, J. Hornegger, P. M. Beckmann, A. Fasching, A. Hartmann, F. Heindl, T. Michel, G. Oezguel, G. Pelzer, C. Rauh, J. Rieger, Z. He, R. Schulz-Wendtland, D. Wachter, E. Wenkel, and C. Riess, "Signal decomposition for x-ray dark-field imaging," in *International Conference on Medical Image Computing and Computer-Assisted Intervention*, P. Golland, N. Hata, C. Barillot, J. Hornegger, and R. Howe, eds. (Springer, 2014), pp. 170–177.
59. S. Reich, T. dos Santos Rolo, A. Letzel, T. Baumbach, and A. Plech, "Scalable, large area compound array refractive lens for hard x-rays," *Appl. Phys. Lett.* **112**(15), 151903 (2018).
60. F. A. Vittoria, G. K. Kallon, D. Basta, P. C. Diemoz, I. K. Robinson, A. Olivo, and M. Endrizzi, "Beam tracking approach for single-shot retrieval of absorption, refraction, and dark-field signals with laboratory x-ray sources," *Appl. Phys. Lett.* **106**(22), 224102 (2015).